International Forum on Aeroelasticity and Structural Dynamics
IFASD 2017
25-28 June 2017 Como, Italy

RECONSTRUCTION OF GUST VELOCITY PROFILES VIA POTENTIAL FLOW, CFD AND ROM TECHNIQUES

Simone Simeone[1], Thomas Rendall[1], Stephen Williams[1], Christopher Wales[1], Jonathan E. Cooper[1], Dorian Jones[1], Ann L. Gaitonde[1]

[1]Department of Aerospace Engineering
University of Bristol
University Walk, Bristol, BS8 1TR, UK
simone.simeone@bristol.ac.uk
thomas.rendall@bristol.ac.uk
stephen.williams@bristol.ac.uk
chris.wales@bristol.ac.uk
j.e.cooper@bristol.ac.uk
dorian.jones@bristol.ac.uk
ann.gaitonde@bristol.ac.uk

Keywords: gust, reconstruction, optimisation, parameterisation, potential flow, CFD, ROM

Abstract: Gust and turbulence events are of primary importance in the estimation of limit loads and in the analysis of flight incidents. Aircraft manufacturers are putting effort into the study of gust reconstruction as it is beneficial during the design stages of the aircraft and for in-service support. The proposed gust reconstruction consists of a numerical optimisation framework where the design variables are parameterised using (and comparing) two methods, namely, Radial Basis Functions and Hick-Henne Bump Functions. Its applications is first demonstrated on a standard flat plate in potential flow using the Unsteady Lumped Vortex Method; then, on the full order model of a typical section of a modern airliner in CFD, using a prescribed velocity approach called the split velocity method (SVM); and, finally, on a reduced order model for the same aerofoil. Results proved satisfactory in all three applications for, but not limited to, the reconstruction of a known one minus cosine gust.

1 INTRODUCTION

Turbulence may be defined as the movement of the air through which an aircraft passes and where any component of the velocity of the air that is normal to the flight path (i.e. gust velocity) will change the effective incidence of the aerodynamic surfaces; in return, this will cause sudden changes in the lift forces and hence a dynamic response of the aircraft involving flexible deformation [1]. Aircraft are expected to encounter atmospheric turbulence (or 'rough air') of varying degrees of severity during their lifecycle; in fact, all modern flight vehicles require the evaluation of dynamic loads in response to discrete and random gust excitation as severe turbulences may affect the static design strength of the aircraft and moderate turbulences may cause fatigue damage to their structure [2, 3]. Moreover, it is a requirement set by the airworthiness authorities [4, 5] that an aeroplane in its design stage must be subjected to symmetrical vertical and lateral gusts in level flight and that the shape of the gust shall be taken as

$$\Omega = \frac{\Omega_{ds}}{2}\left(1 - \cos\frac{\pi s}{H}\right) \qquad \text{for} \qquad 0 \leq s \leq 2H \tag{1}$$

which describes the typical '$1-\cos$' gust; here, H is the gust gradient i.e. the distance parallel to the aeroplane's flight path for the gust to reach its peak velocity, s is the distance penetrated into the gust and Ω_{ds} is the design gust velocity as defined in part (a) of CS-25.341 [5]. The reason behind the choice of the '$1-\cos$' shape appears to be connected with the view that no gust could start with a finite slope; however, as argued by Houbolt [3], this is a notion irrelevant to the assumption that realistic gust encounters could be represented by discrete gusts or, in fact, by any shape. Part (b) of the CS-25.341 regulation also states that the dynamic response of the aeroplane to vertical and lateral *continuous turbulence* must be taken into account.

The purpose of the study presented here is to provide a valid method for the reconstruction of the original gust and/or turbulence experienced by aircraft in service using either data from flight data recorders or from simulations. In fact, understanding the properties of any turbulence encountered by in-service transport aircraft under various operating conditions is of increasing interest to manufacturers, which are putting effort into this process in order to collect valuable information for future aircraft development. The reconstruction of the gust shape would allow a better estimation of the loads exerted on the structure, something that can be of major benefit also for the aircraft operators; in fact, knowing the loads at any location of the aircraft structure during or soon after flight can avoid unnecessary grounding and/or extensive and expensive inspection of the structure. Also, the time interval of regular aircraft inspections can be increased, or these inspections only be conducted on specific parts of the aircraft if information on the loads are readily available, thus reducing operating costs while increasing the availability of the aircraft [6].

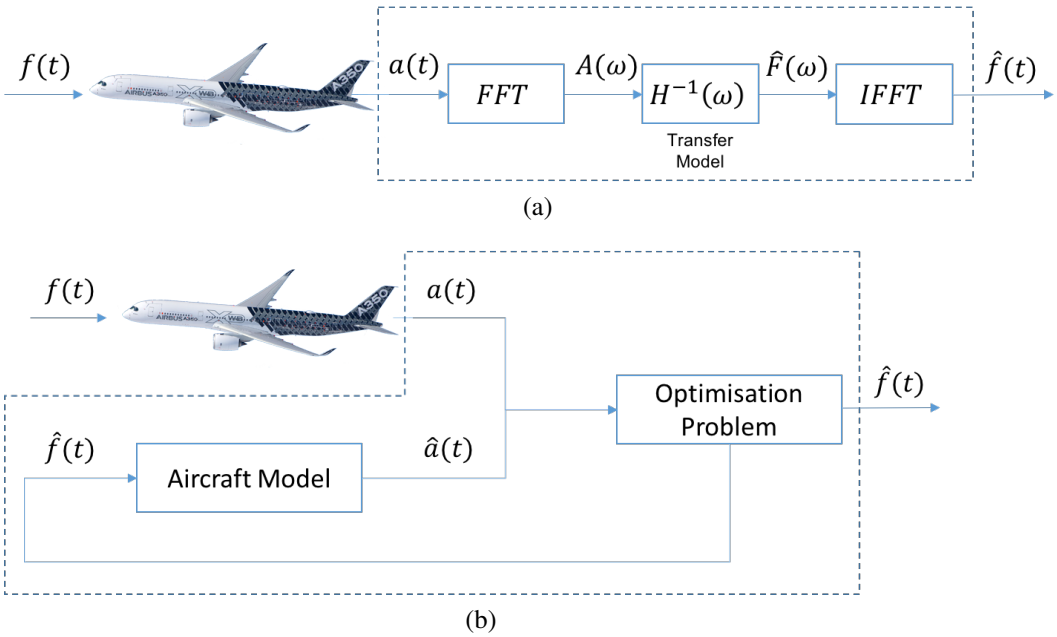

Figure 1: Direct method and optimisation method for force prediction

The earliest approach for gust loads studies dates back to the 40s and 50s [3, 7], with a method known as the discrete-gust approach. This consisted of an analysis of peak vertical accelerations measured by the aircraft flying in gusts; these accelerations were assumed to originate from a series of isolated discrete gusts and were used to derive gust gradient distances and maximum gust velocities. Although this approach was satisfactory for the evaluation of nor-

mal accelerations on future aircraft designs, it was not able to return the real air turbulence [8]. Further efforts were made in the 60*s* and 70*s* on the development of spectral techniques for designing aircraft subject to gust encounters, but the complexity in the definition of the frequency response functions marked a limitation for this technique [3]. In 1999, a Monte-Carlo gust-loads analysis approach was presented by Kim et al [9] in the context of space and missile systems, however the method has limited applicability with a restriction to gust wavelengths greater than 500 ft (152 m). Over the years, force prediction has mainly been done by two methods: the *direct* method and the *optimisation* method [10]. In direct methods, the excitation $f(t)$ is calculated directly from the measured responses $a(t)$ by evaluating the inverse of the forward system model (Figure 1a). Optimisation methods, instead, use a forward model in an optimisation framework where the input to the forward model is tuned until the model responses match the measured responses (Figure 1b); the tuned input is then assumed to equal the original excitation. Although most force prediction methods are of the first type, a shift is ongoing from methods in the frequency domain towards methods in the time domain; this transition is due to the inability of direct methods to capture very time limited events, which play a crucial role in exciting nonlinearities [11]. In 2009, Henrichfreise et al [12] proposed a method consisting of a model-based approach with an observer for a non-linear aircraft model and a disturbance model for the estimation of gusts and structural loads. This method used aircraft motion measurements and parameters already available onboard modern commercial aircraft thus making the estimation of purely monoeuvre-induced structural loads an easy to solve problem; the only unknowns remain the gust velocities which were determined through a non-linear parameter optimisation that computed the gain matrix of the observer model [12]. However, in order to reduce the computational effort required for the convergence of the optimisation problem, only a limited set of elements selected from the gain matrix was considered for the observer feedback.

To remain in line with recent studies, this paper proposes a method for gust reconstruction based on numerical optimisation techniques applied directly to the measurement states of the aircraft (or aerofoil) and introduces a parameterisation for the gust shape using Radial Basis Functions (RBFs) and Hicks-Henne Bump Functions (HHBFs). The method is applied with the fluid modelled using potential flow, the CFD split velocity method (SVM) [13] and reduced order models (ROMs) [14]. The following sections provide an overview of the optimisation framework, followed by a description of the flow solvers and the results obtained for a '$1-\cos$' gust excitation.

2 GUST RECONSTRUCTION METHOD

The system shown in Figure 2 could be defined as a 'black box' where for a given measurement (the input), the original exciting force is extracted (the output). Inside this black box is a framework that includes in its core a numerical optimisation technique that can be wrapped around (virtually) any solver available in academia or industry. Although this system could be potentially applied to any force-prediction application existing in engineering, it is here proposed to reconstruct the gust disturbance profile, and the relative forces exerted on the structure (e.g. lift, moment), of an aircraft that experienced turbulence.

In greater detail, it is assumed that the response of the aircraft to a gust disturbance is available in the form of, for example, a lift coefficient time history (C_ℓ^{target}) or accelerations and that also the initial conditions of the aircraft are known. With these information, the following process applies:

1. An initial guess for the gust shape $\mathbf{\Omega}(\mathbf{x_g})$ is built over an initial set of weighted parametric functions.
2. An aircraft (or aerofoil) model is then required to obtain the time history of the response to the initial (guessed) gust excitation, e.g. $\tilde{C}_\ell(\mathbf{\Omega})$.
3. The resulting time history is then handled by the optimisation algorithm where the cost function is the ℓ^2-norm of the difference between the time history of the model response and the target time history.
4. The optimiser tunes the weights of the parametric functions, i.e. the design variables of the optimisation; each change in the design variables generates a new parametric gust and an additional call to the model/solver.
5. At convergence, when the cost function is minimised, the resulting gust shape is assumed to be the original that caused the target response.

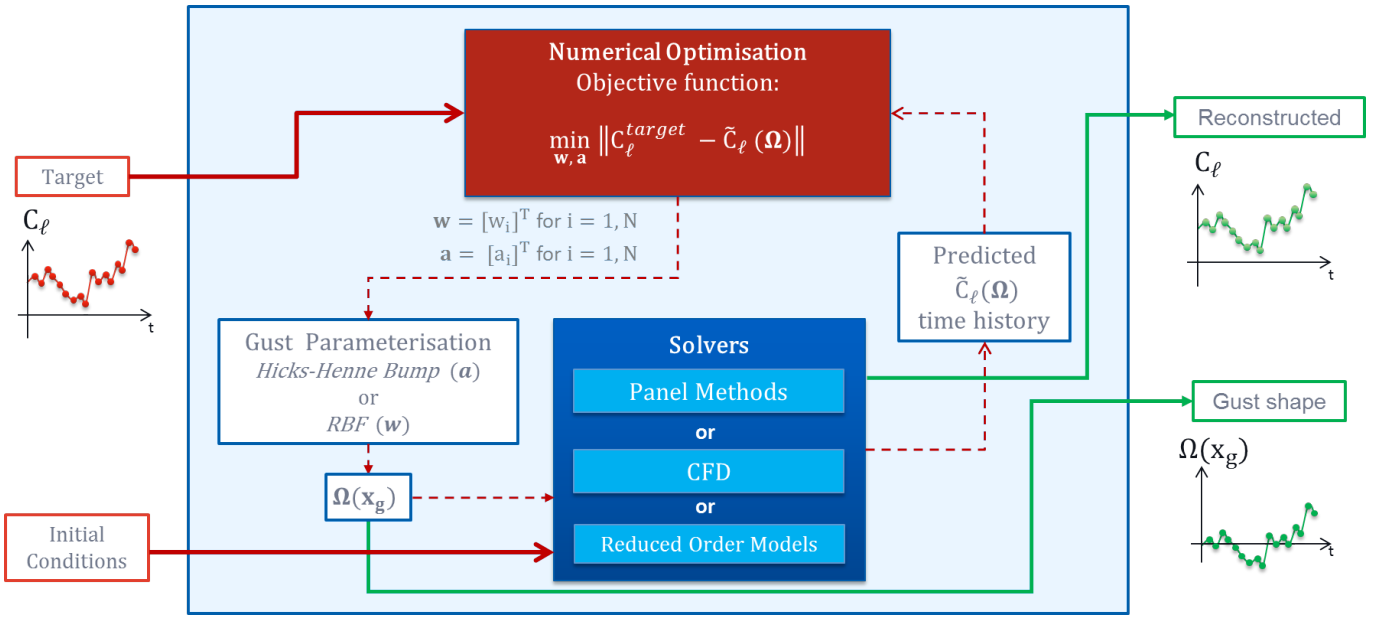

Figure 2: The numerical optimisation framework used for the reconstruction of the gust input profile. Here, C_ℓ is the lift coefficient; $\mathbf{\Omega}$ is the gust function and $\mathbf{x_g}$ the vector of gust points; $\mathbf{w}$ is the vector of the N RBF weights; $\mathbf{a}$ is the vector of the N coefficients for the Hicks-Henne bump functions and N is the number of design variables.

2.1 The Objective Function

For this application, the optimisation can be constructed as an unconstrained problem where the objective function is the ℓ^2-norm of the difference of the measured states of the aircraft and those obtained from a model where the input is the parametrised gust shape $\mathbf{\Omega}$ [15]. As introduced earlier, the objective function for this study is designed around the lift coefficient time history (but accelerations could also be used); hence,

$$\underset{\mathbf{w}}{\text{minimise}} \quad \left|\left| C_\ell - \tilde{C}_\ell(\mathbf{\Omega}) \right|\right|_2 \tag{2}$$

or, explicitly,

$$\underset{\mathbf{w}}{\text{minimise}} \quad \sqrt{\sum_j \left(C_{\ell,j} - \tilde{C}_{\ell,j}(\mathbf{\Omega}) \right)^2} \tag{3}$$

where $\mathbf{w} = [w_i]^T$ is the vector of the weights of the N parametric functions and j counts for each time step. Also, the design variables w_i can be bounded according to the relation

$$w_i^L \leq w_i \leq w_i^U, \qquad \text{for } i = 1, N. \tag{4}$$

where w_i^L and w_i^U are, respectively, the fixed lower and upper boundaries that can be set to significant values, based on experience, or to infinity to leave the problem unbounded. With due modifications, several algorithms can be used to solve this problem and gradient-based optimisation was chosen due to cost of the objective function.

2.1.1 Gradient Evaluation

In order to converge more quickly to the solution, gradient-based optimisation techniques require the gradient of the objective function - i.e. how the states of the aircraft change with respect to the input gust - to be evaluated at any number of iterations.

For simplicity, consider the function of Equation 2

$$f(\mathbf{\Omega}) = C_\ell - \tilde{C}_\ell(\mathbf{\Omega}) \qquad \text{and} \qquad f_j(\mathbf{\Omega}) = C_{\ell,j} - \tilde{C}_{\ell,j}(\mathbf{\Omega}) \tag{5}$$

and define

$$g(\mathbf{\Omega}) = ||f(\mathbf{\Omega})||_2 = \sqrt{\sum_{j=1}^{n} f_j(\mathbf{\Omega})^2}. \tag{6}$$

Differently, the gradient of $g(\mathbf{\Omega})$ can be written as

$$\nabla g(\mathbf{\Omega}) = \frac{1}{2}\left(\sum_j f_j(\mathbf{\Omega})^2\right)^{-\frac{1}{2}}\left(\sum_j 2\, f_j(\mathbf{\Omega})\nabla f_j(\mathbf{\Omega})\right) = \frac{\sum_j f_j(\mathbf{\Omega})\nabla f_j(\mathbf{\Omega})}{||f(\mathbf{\Omega})||_2} \tag{7}$$

or in terms of the Jacobian

$$\nabla g(\mathbf{\Omega}) = \frac{J_f(\mathbf{\Omega})^T\, f(\mathbf{\Omega})}{||f(\mathbf{\Omega})||_2} \tag{8}$$

where $J_f(\mathbf{\Omega})^T$ is the Jacobian matrix of $f(\mathbf{\Omega})$. The conventional method for finding this gradient is numerically via finite difference approximation, where a pre-determined Δw_i is sequentially added/subtracted to each weight of the parametric functions and its influence measured over the entire profile (Figure 3).

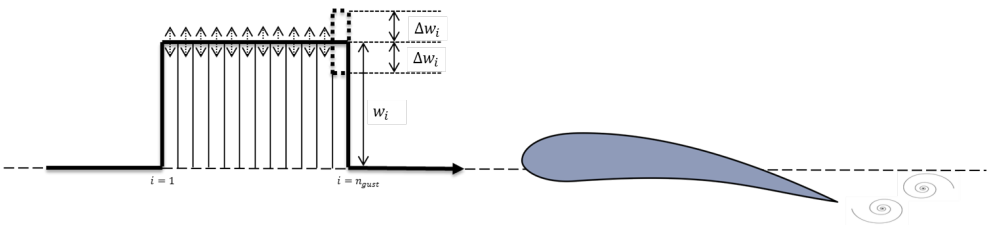

Figure 3: Representation of finite difference approximation.

2.2 Gust Shape Parameterisation

In aerodynamics, generally, shape parameterisation concerns the way the aerofoil geometry is handled and deformed by an optimisation algorithm, and determines both the fidelity and range of control available. In the context of this study, instead, shape parameterisation is adapted and applied to gust profiles in order to achieve a satisfactory deformation of the initial guessed gust during the iterative optimisation process. Two parameterisation methods have been considered and their effectiveness and efficiency have been measured on the ability to cover a large design space with a limited set of design variables, as suggested by the work of Masters et al [16]. Recalling the first step of the optimisation process, where an initial guess for the gust is required, it becomes natural to assume that deformative methods are the best candidates for this type of application. In fact, deformative methods consist in the generation of a new shape following the deformation of a preliminary, assumed, shape. The two deformative methods considered here are Hicks-Henne bump functions (analytical method) and Radial Basis Functions (free-form deformation method), and are introduced in the following sections.

2.2.1 Hicks-Henne Bump Functions

Hicks-Henne bump functions use a base shape definition over which a linear combination of N basis functions defined between 0 and 1 is added to obtain the desired shape (Figure 4). Applied to gust shapes, these can be written as

$$\Omega(\mathbf{x_g}) = \mathbf{\Omega}^{initial} + \sum_{i=1}^{N} a_i \phi_i(\mathbf{x_g}) \tag{9}$$

where a_i are the coefficients of the N basis functions. These are defined as

$$\phi_i(\mathbf{x_g}) = \sin^{t_i}\left(\pi \mathbf{x_g}^{\ln(0.5)/\ln(h_i)}\right), \tag{10}$$

as proposed by Hicks and Henne [17]. In Equation 10, h_i is the location of the maxima of the basis functions and is defined as

$$h_i = \frac{1}{2}\left[1 - \cos\left(\frac{i\pi}{N+1}\right)\right], \qquad i = 1, \ldots, N \tag{11}$$

whereas t_i controls the width of the functions and can be set equal to a constant [18]. Although for this study only a_i is set as the design variable for the optimisation, in general all parameters controlling the shape functions (i.e. a_i, t_i and h_i) can be defined as design variables [16].

2.2.2 Radial Basis Functions

The Radial Basis Functions (RBFs) approximation (Figure 5) is built upon the summation of N basis functions that are (usually) defined by the Euclidean norm of a known set of points - the control points, also defined as the RBF centres $\mathbf{c} = [c_i^T]$ - and the variables at which the approximation is sought - the gust points $\mathbf{x_g}$. RBFs evaluate the value of the interpolation at any point in space by a weighted influence of the value at every control point; the influence is determined by the vector distance of the evaluation point from all the control points. Here, the RBF approximation can be expressed as

$$\Omega(\mathbf{x_g}) = \sum_{i=1}^{N} w_i \phi(||\mathbf{x_g} - \mathbf{c}_i||) + p(\mathbf{x}) \tag{12}$$

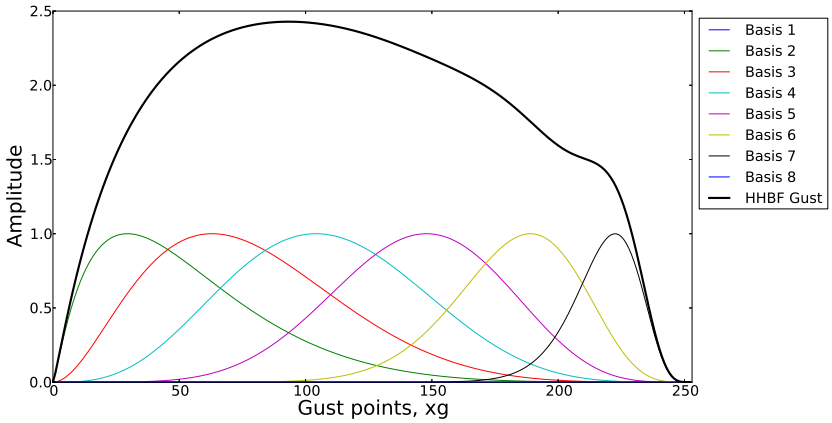

Figure 4: Example of Hicks Henne Bump Functions parameterisation with 8 basis functions

where $\phi(||.||)$ are the N 'radius' functions, which in this work are of the Gaussian type (i.e. $\phi(||.||) = e^{-(\epsilon||.||)^2}$) but can likewise be of different nature (e.g. quadratic, inverse quadratic, one-minus-cos, etc.), w_i are N scalar variables, also known as weights of the basis functions, and $p(\mathbf{x})$ is an (optional) added polynomial used to ensure that translation of the gust shape is captured without added deformation. The centres $\mathbf{c} = [c_i^T]$ are defined by the initial guess of the gust shape. When using this parameterisation method within the gust reconstruction framework, the vector of weights $\mathbf{w}$ and the polynomial coefficients are the design variables of the optimisation problem.

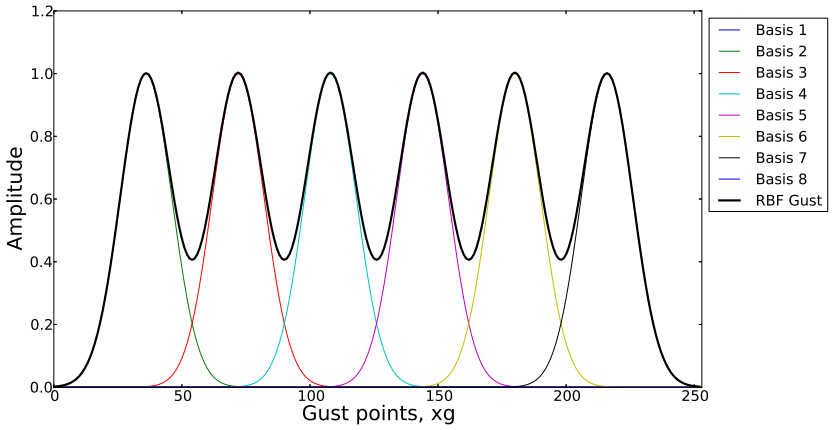

Figure 5: Example of RBF parameterisation with 8 basis functions

2.3 Aerodynamic Solvers

The three aerodynamic models used for this work are briefly described below. These are the unsteady lumped vortex method (ULVM), which uses an aerofoil idealised as a flat plate, computational fluid dynamics (CFD) with the aerofoil of a typical modern commercial aircraft and, finally, a reduced order model (ROM) of the same aerofoil.

2.3.1 Unsteady Lumped Vortex Method

The lumped vortex method is based on the surface distribution of singularity elements (lumped vortices) where the solution is reduced to finding their strengths. This approach is more economical from the computational point of view compared to those methods that solve for the

flowfield in the whole fluid volume e.g. finite-difference methods. Figure 6 shows a representation of a two-component idealised aerofoil with two lumped vortices (singularity elements) and two collocation points (i.e. where the boundary conditions need to be enforced). In addition, there is a wake model behind the trailing edge. The lumped vortices are located at the 1/4-chord

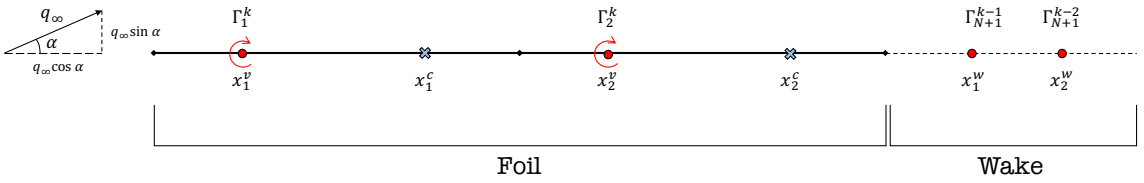

Figure 6: Representation of a two-component idealised aerofoil with vortices and control points, and with a wake. The superscript c indicates a collocation point, k the time level, v a vortex point and w a wake point.

point (centre of pressure) of each component of the flat plate and the collocation points at the 3/4-chord of each component; this configuration matches thin aerofoil theory which satisfies the Kutta condition at the trailing edge of the flat plate [19]. The boundary condition requires that the normal velocity component must be zero at the collocation points. The net upwash (y-component of velocity) induced by all the aerofoil vortices at a generic control point m is given by

$$v_m = \sum_{n=1}^{N} \frac{\Gamma_n}{2\pi(x_n^v - x_m^c)} \tag{13}$$

In order to satisfy the flow tangency condition, the net upwash must be balanced by the downwash (velocity in the negative y-direction) induced by the freestream ($q_\infty \sin\alpha$) and the incident gust (Ω_k)

$$\sum_{n=1}^{N} \frac{\Gamma_n}{2\pi(x_n^v - x_m^c)} = -\Omega_k - q_\infty \sin\alpha \tag{14}$$

Furthermore, Kelvin's condition states that the total circulation about the aerofoil and its shed vortex wake must remain constant; this condition is also known as the conservation of circulation and translates mathematically to

$$\sum_{n=1}^{N+1} \Gamma_n(t) = \sum_{n=1}^{N} \Gamma_n(t - \Delta t) \qquad \text{i.e.} \qquad \frac{d\Gamma}{dt} = 0 \tag{15}$$

where Γ_{N+1} is the circulation of the shed vortex and $\sum_{n=1}^{N} \Gamma_n(t - \Delta t)$ is the total circulation on the aerofoil at the previous time step. This system of equations can be expressed in matrix form as $[\mathbf{A}]\{\mathbf{\Gamma}\} = \{\mathbf{b}\}$, with

$$[\mathbf{A}] = \frac{1}{2\pi}\begin{bmatrix} \frac{1}{x_1^v - x_1^c} & \frac{1}{x_2^v - x_1^c} & \cdots & \frac{1}{x_N^v - x_1^c} & \frac{1}{x_{N+1}^v - x_1^c} \\ \frac{1}{x_1^v - x_2^c} & \frac{1}{x_2^v - x_2^c} & \cdots & \frac{1}{x_N^v - x_2^c} & \frac{1}{x_{N+1}^v - x_2^c} \\ \vdots & \vdots & \ddots & \vdots & \vdots \\ \frac{1}{x_1^v - x_N^c} & \frac{1}{x_2^v - x_N^c} & \cdots & \frac{1}{x_N^v - x_N^c} & \frac{1}{x_{N+1}^v - x_N^c} \\ 1 & 1 & \cdots & 1 & 1 \end{bmatrix}, \{\mathbf{b}\} = -\Omega_k - q_\infty \sin\alpha \begin{bmatrix} 1 \\ 1 \\ \vdots \\ 1 \\ 0 \end{bmatrix} - \sum_{n=1}^{N} \Gamma_n(t - \Delta t) \tag{16}$$

$[\mathbf{A}]$ is often referred to as *influence coefficient* matrix. In order to take into account the upwash induced by the wake vortices and to include the wake vortices in the total circulation, the above system must be modified. In fact, Equation 16 is solved at the first time step only, when no

vortices have been shed in the wake; for the following time steps the influence coefficient matrix remains the same but the right hand side changes to

$$\{\mathbf{b}\} = \begin{Bmatrix} -q_\infty \sin\alpha - \Omega_1^k - \sum_{i=1}^{k-1} \frac{\Gamma_{N+1}^{k-i}}{2\pi(x_i^w - x_1^c)} \\ -q_\infty \sin\alpha - \Omega_2^k - \sum_{i=1}^{k-1} \frac{\Gamma_{N+1}^{k-i}}{2\pi(x_i^w - x_2^c)} \\ \vdots \\ -q_\infty - \Omega_N^k - \sum_{i=1}^{k-1} \frac{\Gamma_{N+1}^{k-i}}{2\pi(x_i^w - x_N^c)} \\ -\sum_{n=1}^{N} \Gamma_n(t - \Delta t) \end{Bmatrix} \tag{17}$$

Once the strengths of the lumped vortices have been evaluated, the lift can be obtained. For the unsteady case, the Kutta-Jukowski law $L = \rho U_\infty \Gamma$ would not be sufficient to evaluate the total lift experienced by the aerofoil as it would give a zero lift for the initial time step of a transient solution. This is because at this step the lift is due to the acceleration of the flow rather than the net circulation about the aerofoil. Hence, the unsteady Bernoulli equation must be used to obtain the unsteady pressure and lift. As a result, it can be demonstrated [19] that the unsteady lift at each time step k is given by

$$L_k = \rho U_\infty \sum_{n=1}^{N+1} \Gamma_n^k + \rho \sum_{n=1}^{N} \left(\frac{\Delta\phi_n^k - \Delta\phi_{n-1}^{k-1}}{\Delta t} \right) \Delta x \tag{18}$$

where ϕ is the velocity potential of the perturbation flowfield. From this equation it is clear that the first term accounts for the lift due to the steady flow (as expected from the Kutta-Jukowski theorem) and the second term accounts for the unsteady effects. The nondimensional lift coefficient is then $C_l = \frac{L}{\frac{1}{2}\rho q_\infty^2 c}$.

2.3.2 CFD: Split Velocity Method

The potential flow approach described in the previous section does not allow for transonic effects, or other aerodynamic nonlinearities effects such as high angles of attack, to be captured during a gust encounter. This limitation makes the reconstruction of a gust profile impracticable for such cases and, indeed, a CFD analysis is required. Typically, the most direct way to introduce a gust into a CFD code is the modification of the boundary conditions at the far field of the computational domain. However, this application requires a very fine mesh to be defined all the way from the body to the far field in order not to dissipate the effects of the disturbances; as a result, the computational cost for such a simulation is very high and its usage very limited. In order to overcome this issue, Wales et al [13] recently proposed a solution based on the decomposition of the velocity components of the Euler equations into a prescribed gust velocity term and the remaining velocity components. Known as the split velocity method (SVM), this method is able to capture the full interaction between the body and the gust as no simplifying assumptions are made in the solution of the Euler equations. Moreover, the computational cost is reduced by the usage of a coarse mesh away from the body, because this does not dissipate the effects of the gust and its motion, which are prescribed. Hence, starting from the unsteady two-dimensional (2-D) version of the Euler equations, which can be rewritten as

$$\frac{\partial}{\partial t} \begin{bmatrix} \rho \\ \rho u \\ \rho v \\ \rho E \end{bmatrix} + \frac{\partial}{\partial x} \begin{bmatrix} \rho u \\ \rho u^2 + p \\ \rho uv \\ (\rho E + p)u \end{bmatrix} + \frac{\partial}{\partial y} \begin{bmatrix} \rho v \\ \rho uv \\ \rho v^2 + p \\ (\rho E + p)v \end{bmatrix} = 0 \tag{19}$$

with

$$p = \rho(\gamma - 1)\left[E - \frac{1}{2}(u^2 + v^2)\right], \tag{20}$$

the velocity and energy can be decomposed as

$$u = \tilde{u} + u_g \qquad v = \tilde{v} + v_g \qquad E = \tilde{E} + E_g \tag{21}$$

where u_g and v_g are the prescribed gust velocity components, and the split of the total energy is defined by the decomposition

$$\begin{aligned} E &= \frac{p}{\rho(\gamma-1)} + \frac{1}{2}(u^2 + v^2) \\ &= \underbrace{\frac{p}{\rho(\gamma-1)} + \frac{1}{2}(\tilde{u}^2 + \tilde{v}^2)}_{\tilde{E}} + \underbrace{(\tilde{u}u_g + \tilde{v}v_g) + \frac{1}{2}(u_g^2 + v_g^2)}_{E_g}. \end{aligned} \tag{22}$$

By substituting the terms defined in Equation 21 into Equations 19 and 20 and with further algebra manipulation - where the applied gust is separated from the rest of the solution - it can be shown [20] that the Euler equations can be rewritten as

$$\frac{\partial}{\partial t}\begin{bmatrix}\rho\\ \rho\tilde{u}\\ \rho\tilde{v}\\ \rho\tilde{E}\end{bmatrix} + \frac{\partial}{\partial x}\begin{bmatrix}\rho(\tilde{u}+u_g)\\ \rho\tilde{u}(\tilde{u}+u_g)+p\\ \rho\tilde{v}(\tilde{u}+u_g)\\ \rho\tilde{E}(\tilde{u}+u_g)+p\tilde{u}\end{bmatrix} + \frac{\partial}{\partial y}\begin{bmatrix}\rho(\tilde{v}+v_g)\\ \rho\tilde{u}(\tilde{v}+v_g)\\ \rho\tilde{v}(\tilde{v}+v_g)+p\\ \rho\tilde{E}(\tilde{v}+v_g)+p\tilde{v}\end{bmatrix} + \begin{bmatrix}0\\ s_m(u_g)\\ s_m(v_g)\\ s_e(u_g,v_g)\end{bmatrix} = 0 \tag{23}$$

where

$$p = \rho(\gamma - 1)\left[\tilde{E} - \frac{1}{2}(\tilde{u}^2 + \tilde{v}^2)\right], \tag{24}$$

and the source terms are

$$s_m(u_g) = \rho\left[\frac{\partial u_g}{\partial t} + (\tilde{u}+u_g)\frac{\partial u_g}{\partial x} + (\tilde{v}+v_g)\frac{\partial u_g}{\partial y}\right] \tag{25}$$

$$s_m(v_g) = \rho\left[\frac{\partial v_g}{\partial t} + (\tilde{u}+u_g)\frac{\partial v_g}{\partial x} + (\tilde{v}+v_g)\frac{\partial v_g}{\partial y}\right] \tag{26}$$

$$s_e(u_g, v_g) = \tilde{u}s_m(u_g) + \tilde{v}s_m(v_g) + p\left(\frac{\partial u_g}{\partial x} + \frac{\partial v_g}{\partial y}\right). \tag{27}$$

Equations 23 are solved in integral form on a fixed mesh such that

$$\frac{d}{dt}\iint_\Omega \boldsymbol{W}\, dx\, dy + \int_{\partial\Omega}(\boldsymbol{F}\, dy - \boldsymbol{G}\, dx) + \iint_\Omega \boldsymbol{S}\, dx\, dy = 0 \tag{28}$$

where

$$\begin{aligned} \boldsymbol{W} &= [\rho,\ \rho\tilde{u},\ \rho\tilde{v},\ \rho\tilde{E}]^T \\ \boldsymbol{F} &= [\rho(\tilde{u}+u_g),\ \rho\tilde{u}(\tilde{u}+u_g)+p,\ \rho\tilde{v}(\tilde{u}+u_g),\ \rho\tilde{E}(\tilde{u}+u_g)+p\tilde{u}] \\ \boldsymbol{G} &= [\rho(\tilde{v}+v_g),\ \rho\tilde{u}(\tilde{v}+v_g),\ \rho\tilde{v}(\tilde{v}+v_g)+p,\ \rho\tilde{E}(\tilde{v}+v_g)+p\tilde{v}] \\ \boldsymbol{S} &= [0,\ s_m(u_g),\ s_m(v_g),\ s_e(u_g,\ v_g)] \end{aligned} \tag{29}$$

However, it can be shown that the SVM equations (24, 28 and 29) can be solved on a moving mesh code by adding the source terms to the moving grid equations and setting the grid velocities equal to the negative gust velocities. Indeed, Wales et al used a modified version of a

moving mesh Euler code to demonstrate the efficacy of their method [13]; and this exact solver was used for this study. The aerofoil model used here is shown in Figure 7 and represents a typical section of a modern commercial aircraft [21]. Figure 8a and 8b show, respectively, a snapshot of the forward velocity contour plot at zero angle of attack in steady conditions and during a gust encounter.

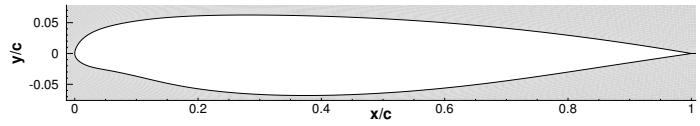

Figure 7: FFAST crank aerofoil

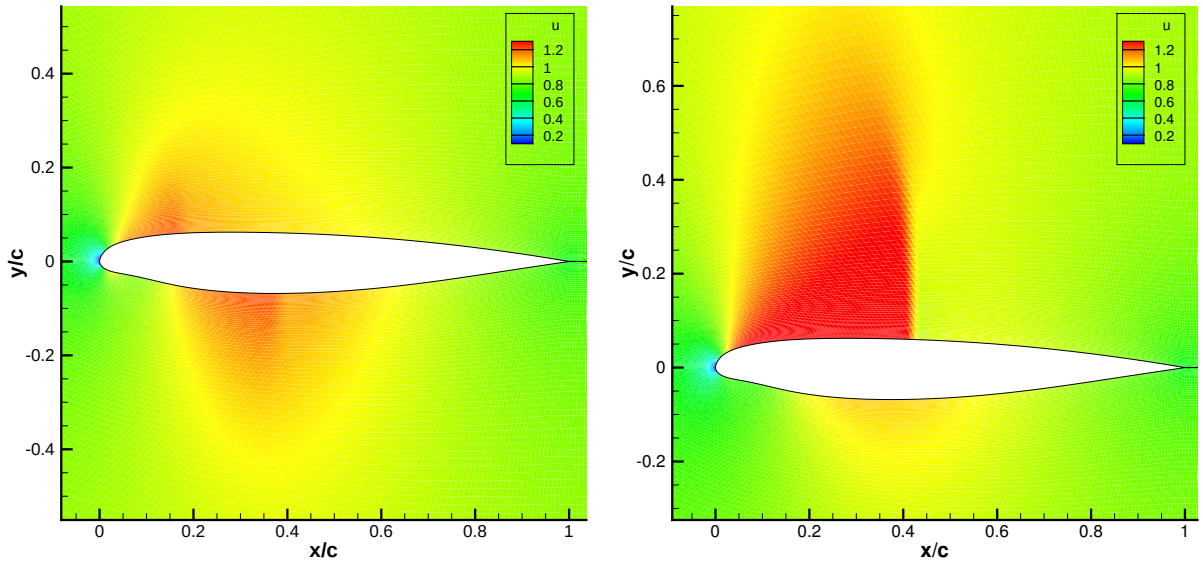

(a) (b)

Figure 8: Forward velocity contour plot of aerofoil at zero angle of attack in steady conditions (a) and during gust encounter (b) for $M = 0.73466$ and $Re \approx 1.43 \times 10^8$.

2.3.3 Reduced Order Model

CFD analyses are required to capture the detail of the flow behaviour, however low computational costs are essential during the early stages of the design of an aircraft, which restricts their use. Reduced order models (ROMs) attempt to capture the dominant dynamic behaviour of an unsteady CFD code, but at lower computational cost. In gust design applications, suitable ROMs could provide the aircraft response to gust and turbulence encounters, in order to extract the critical gust loads that are fundamental for sizing the aircraft. Williams et al [14] recently demonstrated that a very efficient gust ROM can be achieved without loosing the accuracy of the results obtained with full order simulations. Undeniably, the rapidity and maintained accuracy of ROMs represents an invaluable characteristic in the gust reconstruction framework.

The ROM in this work is built from a single sharp-edged gust, of magnitude 1 m/s, alongside a small number of steady simulations of various angles of attack. An effective step-down response can be produced by subtracting the sharp-edged gust response from the steady data (with the same angle of attack as the sharp-edged gust starts with) [22]. This step-down response is then

used within an Eigensystem Realisation Algorithm (ERA) to perform a system reduction to calculate the system matrices of a reduced order, discrete state-space model [20, 23], which can be used to express the near-linear behaviour of the given system. To ensure the ROM is stable (all eigenvalues have a magnitude of less than 1) restarting [24] and/or Schur decomposition [25] can be used. Once the system matrices have been calculated, they are valid for any gust of given Mach number and Reynolds number. However, they can also be extended to calculate the system response at any altitude. The computational cost of calculating a gust response once the matrices have been calculated is negligible. For a more detailed breakdown of the ROM, see Williams et al [14, 22].

3 RESULTS

3.1 Case Study: '$1 - \cos$' gust

The reconstrution of a typical '$1 - cos$' gust was considered for this study. The expression governing the behaviour of this gust (Figure 9) is given as a function of time in the form

$$\Omega(t) = \frac{\Omega_0}{2}\left(1 - \cos\frac{2\pi V}{h_g}t\right) \tag{30}$$

where Ω_0 is the value of the maximum gust velocity, V is the freestream velocity and h_g is the length of the gust (i.e. twice the gradient H). This analytical function was used to generate the target lift response (C_ℓ^{target}) for all the three optimisation cases, as discussed in the next sections.

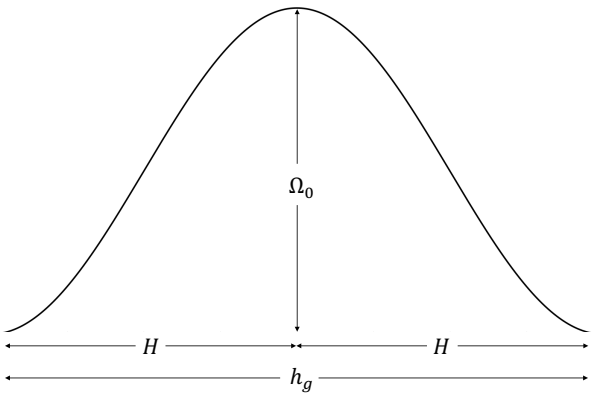

Figure 9: Typical '$1 - \cos$' gust shape with dimensions.

3.2 Gust reconstruction with ULVM

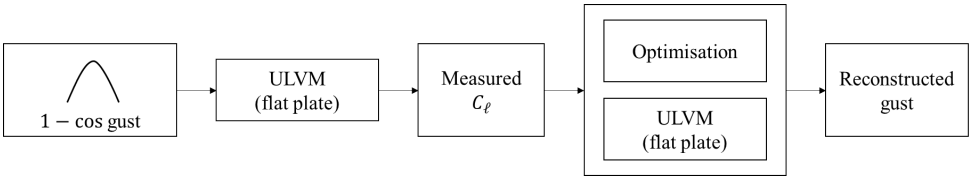

Figure 10: Gust reconstruction diagram

The diagram of Figure 10 helps to better understand the components required for this application. The ULVM was used to compute the lift coefficient time history of a flat plate undergoing a

'$1-\cos$' gust with normalised maximum velocity $\Omega_0 = 0.15$ and width 5 times greater than the chord ($h_g = 5c$). The C_ℓ time history was then provided as measured data to the reconstruction framework detailed in Figure 2, which was designed around the ULVM for this case. The reconstructed gust is the outcome of the iterative process and is compared in Figures 11a and 11c to the reference '$1-\cos$' gust obtained analytically. Figure 11a shows the results obtained using the RBF parameterisation, whilst Figure 11c the results obtained using Hicks-Henne Bump Functions. In both cases, the Sequential Least Squares Programming (SLSQP) algorithm[1] was used for the optimisation. When using RBF parameterisation, the optimisation converged in approximately 20 minutes requiring 26 objective function evaluations and 4 gradient evaluations; however, Figure 11a shows that the initial and final zero-velocity gust points, along with the peak, were not well matched by the reconstruction. These resulted in a negative C_ℓ at the impact time and a small discrepancy at the peaks, as shown in Figure 11b. With the HHBF parameterisation, instead, the optimisation took longer to converge (~ 2 hours) as 207 objective function evaluations were required, along with 29 gradient evaluations. However, Figure 11c shows that a better reconstruction was achieved, as both the zero-velocity gust points and the peak were perfectly matched; this resulted in a nearly perfect match for the reconstructed C_ℓ time history (Figure 11d). Neither constraints nor bounds were set on the design variables for this optimisation problem.

3.3 Gust reconstruction in CFD

A '$1-\cos$' gust shape with characteristics similar to the potential flow case but with a dimensional maximum velocity of $\Omega_0 = 15.623\ m/s$ and width $h_g = 15c$ was given as input to the CFD model described in Section 2.3.2 to generate the target C_ℓ time history for the optimisation (Figure 12). The flow initial conditions were $M = 0.73466$ and $Re \approx 1.43 \times 10^8$. As before, Figures 13a to 13d show the reconstructed gust and C_ℓ time histories compared to the simulation target. For this CFD case, a good match was achieved when employing the RBF parameterisation (Figure 13a), with a slight discrepancy at the initial and final zero points and at the peak. When using the HHBF method, instead, a perfect match was achieved (Figure 13c). Clearly, CFD analyses are much more expensive than the potential flow approach; however, as mentioned earlier, they become essential when analysing the effects of aerodynamic nonlinearities. The SLSQP optimisation algorithm required approximately 40 hours to converge, yet only 14 function calls and 9 gradient evaluations. Although no constraints were set for this optimisation problem, bounds on the design variables (i.e. the weights of the parametric functions) were necessary to guarantee the convergence of the CFD code.

3.4 Gust reconstruction with ROMs

Similarly to the two previous cases, the diagram of Figure 14 summarises the gust reconstruction routine. However, before the process could start, a ROM of the FFAST crank aerofoil of Figure 7 was built for $M = 0.73466$ at sea level conditions, according to the procedure described in Section 2.3.3.

The optimisation converged in under a minute when using either RBFs ($\sim 55\ s$) or the HHBFs ($\sim 40\ s$) and a perfect match was achieved in the reconstruction of the C_ℓ time histories, as

[1]SLSQP optimiser is a sequential least squares programming algorithm which uses the Han-Powell quasi-Newton method with a BFGS update of the B-matrix and an L1-test function in the step-length algorithm. The optimizer uses a slightly modified version of Lawson and Hansons nonlinear least-squares (NNLS) solver [26].

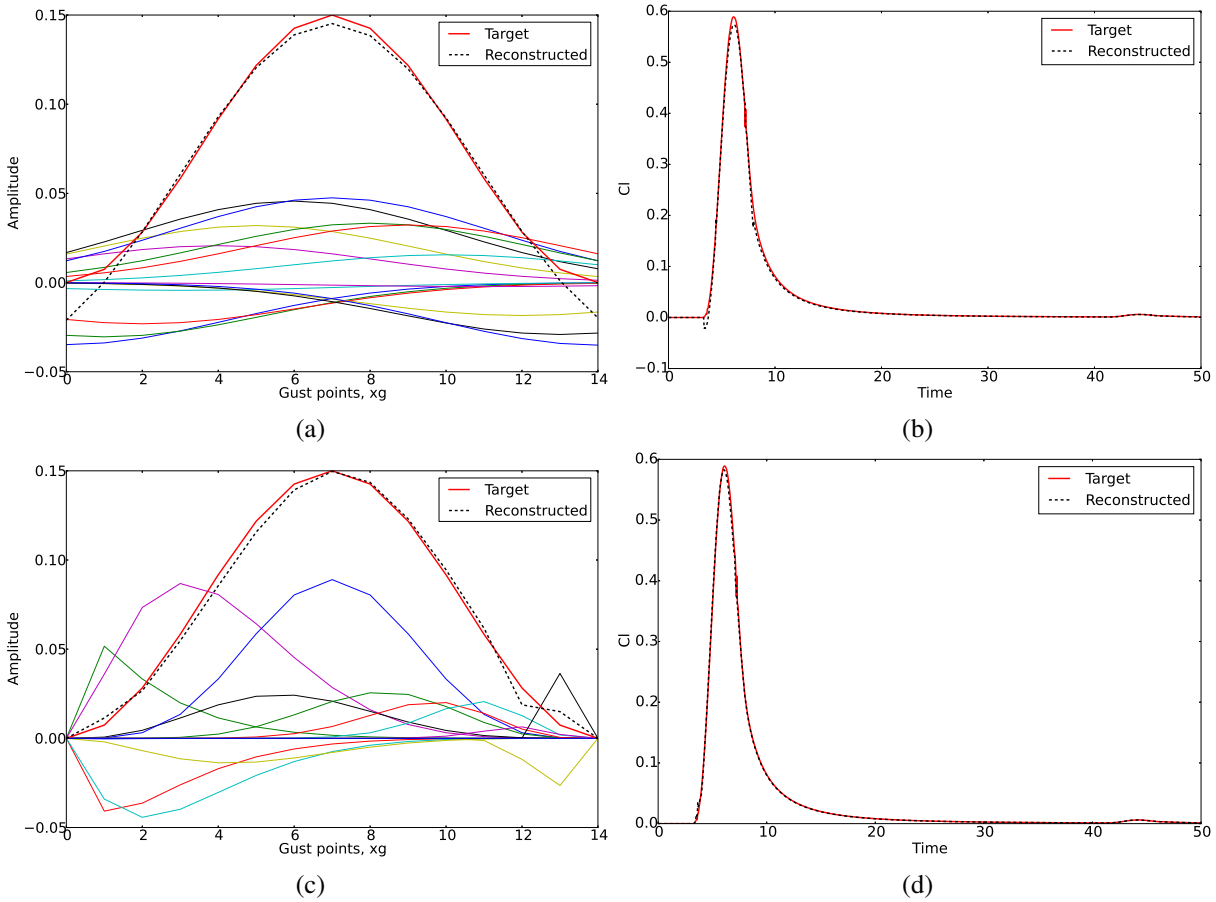

Figure 11: Reconstruction of gust profiles for a flat plate obtained with the SLSQP optimisation algorithm. Figures (a) and (b) show, respectively, the reconstructed gust and the resulting lift coefficient using 15 RBFs for the parameterisation. Figures (c) and (d) show, respectively, the reconstructed gust and the resulting lift coefficient using, instead, 15 HHBFs for the parameterisation.

shown in Figures 15b and 15d. In terms of parameterisation performance, Figure 15a shows that, for the reconstruction of the gust, 18 radial basis functions with 600 cost function calls were required to achieve the same accuracy obtained with only 8 bump functions and 489 function calls. The higher number of function calls required to reach convergence are due to the reduced tolerance of the objective function ($O(10^{-7})$), which is set as one of the stop criteria. As previously and with both parameterisation methods, the SLSQP algorithm was used for the optimisation. Neither constraints nor bounds were set on the design variables for this case.

4 CONCLUSIONS

This work focuses on three objectives. The first is to demonstrate the applicability of the gust reconstruction framework to three flow solvers of different nature i.e. potential flow (ULVM), CFD (taking advantage of the split velocity method) and reduced order models. In fact, any type of model is a suitable candidate as little or no knowledge of the underlying equations is needed, except from the simple input/output manipulation of the main routine. The second objective is to compare the performance and efficiency of two parameterisation methods applied to the design variables of the optimisation (the gust input velocities); these are Radial Basis Functions and Hicks-Henne Bump Functions. In order to address the first two objectives, the cost function was designed to minimise the difference between the reference and the reconstructed lift

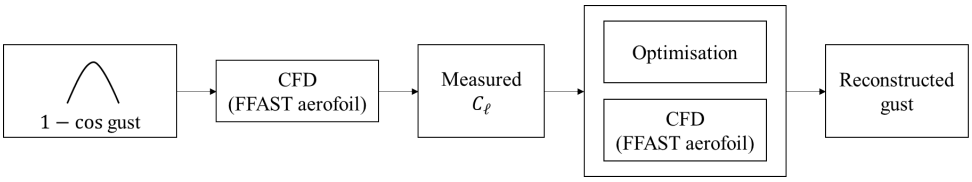

Figure 12: Gust reconstruction diagram

coefficient time histories, by tuning the weights for the RBFs or the HHBFs. Results obtained with the SLSQP optimisation algorithm have shown that a good agreement was achieved in all the three applications, with the HHBF parameterisation performing generally better than the RBFs. Although, the well-known '$1 - \cos$' gust shape was used as the pilot case, this approach shall be valid for any arbitrary gust [27] and, once again, the results obtained have proven that optimisation represents an invaluable solution for the reconstruction of the forces experienced by an aircraft in turbulent atmospheric conditions.

The third objective reflects a medium-term development of the gust reconstruction framework for near real-time analysis. In fact, ROMs have proven a valid choice for this type of application, as their major cost is in the model generation phase and not in their use. As a result, this allows a quick, efficient and more accurate reconstruction process, which has the potential to be exploited as a technology for instantaneous monitoring of the airframe in flight, thus minimising (or avoiding) the need for further aircraft inspections.

5 REFERENCES

[1] Wright, J. R. and Cooper, J. E. (2007). *Introduction to Aircraft Aeroelasticity and Loads*. Wiley.

[2] Hoblit, F. M. (1988). *Gust Loads on Aircraft: Concepts and Applications*. AIAA Education Series, AIAA, Washington, DC.

[3] Houbolt, J. C. (1973). Atmospheric Turbulence. *AIAA Journal*, 11 (04), 421–437.

[4] (1994). Joint aviation requirements - jar-25 large aeroplanes. Federal Aviation Regulations. Change 14 - Book 1 - Subpart B.

[5] (2007). Certification specifications for large aeroplanes cs-25. European Aviation Safety Agency. Section 1 - Subpart C.

[6] Bensch, L., Henrichfreise, H., Gusset, J., et al. (2007). Method for reconstructing gusts and structural loads at aircraft, in particular passenger aircraft. World Intellectual Property Organization.

[7] Houbolt, J. C. (1970). Design Manual for Vertical Gusts Based on Power Spectral Techniques. *Air Force Flight Dynamics Lab (AFFDL-TR-70-106)*.

[8] Zbrozek, J. K. (1961). The Relationship between the Discrete Gust and Power Spectra Presentations of Atmospheric turbulence, with a suggested Model of Low-Altitude Turbulence. *Aeronatucial Research Council Reports and Memoranda*, R. & M. No. 3216.

[9] Kim, M. C., Kabe, A. M., and Lee, S. S. (1999). Atmospheric Flight Gust Loads Analysis. *Space and Missile Systems Center Air Force Materiel Command*, TR-99(1534)-5.

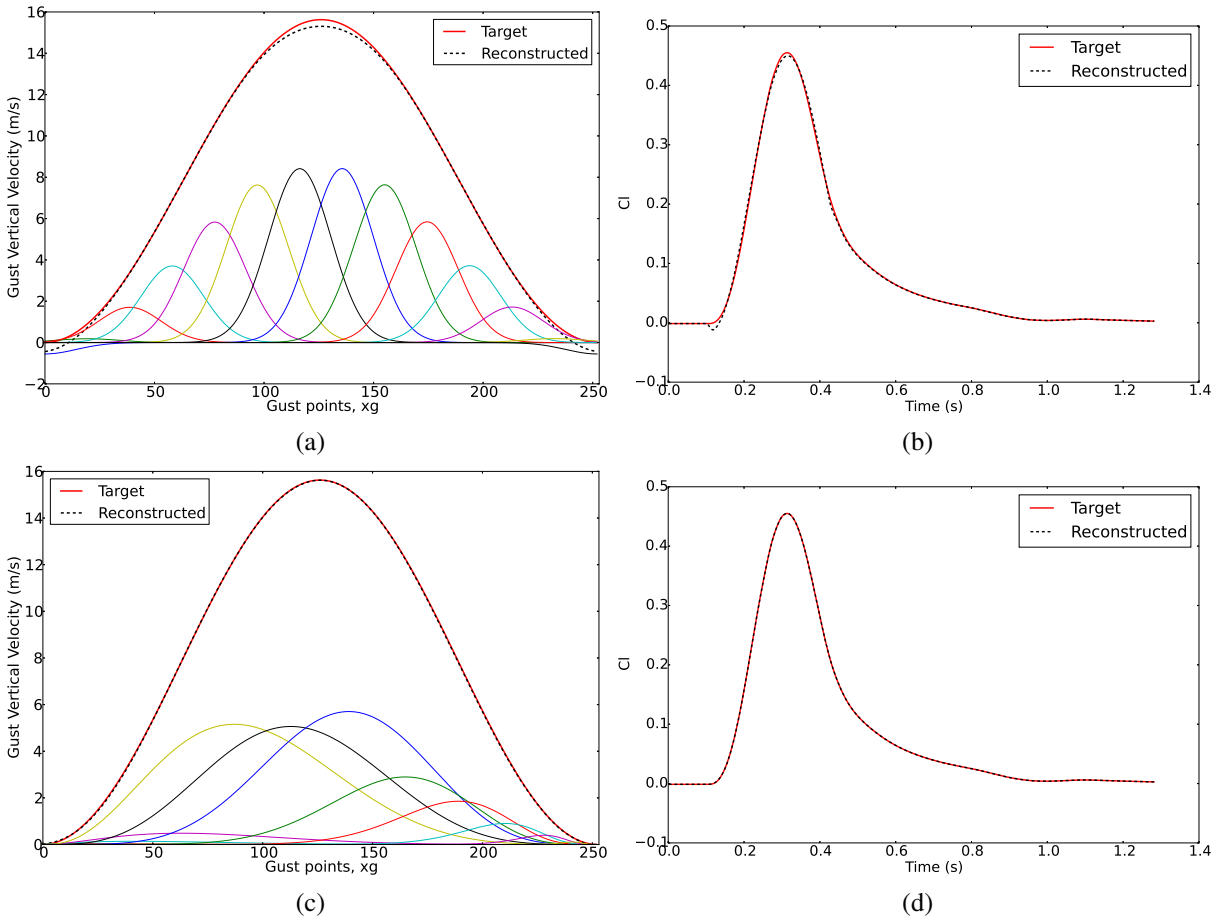

Figure 13: Reconstruction of gust profiles for the FFAST crank aerofoil obtained with the SLSQP optimisation algorithm. Figures (a) and (b) show, respectively, the reconstructed gust and the resulting lift coefficient using 14 RBFs for the parameterisation. Figures (c) and (d) show, respectively, the reconstructed gust and the resulting lift coefficient using, instead, 14 HHBFs for the parameterisation.

[10] Wang, B.-T. (2002). Prediction of Impact and Harmonic Forces Acting on Arbitrary Structures: Theoretical Formulation. *Mechanical Systems and Signal Processing*, 16(6), 935–953. ISSN 08883270. doi:10.1006/mssp.2002.1505.

[11] Nordberg, P. (2004). *Time Domain Methods for Load Identification of Linear and Nonlinear Systems*. Doktorsavhandlingar vid Chalmers tekniska. Ny serie, no: 2170. Department of Applied Mechanics, Chalmers University of Technology,. ISBN 91-7291-489-0.

[12] Henrichfreise, H., Bensch, L., Jusseit, J., et al. (2009). Estimation of gusts and structural loads for commercial aircraft. In *Int. Forum on Aeroelasticity and Structural Dynamics (IFASD)*. Seattle, USA: IFASD, pp. 1–11.

[13] Wales, C., Jones, D., and Gaitonde, a. (2015). Prescribed Velocity Method for Simulation of Aerofoil Gust Responses. *Journal of Aircraft*, 52(1), 1–13. ISSN 0021-8669. doi: 10.2514/1.C032597.

[14] Williams, S. P., Jones, D., Gaitonde, A., et al. (2016). Application of Reduced Order Models in Aircraft Gust Response Studies. *46th AIAA Fluid Dynamics Conference*, (June), 1–23. doi:10.2514/6.2016-4261.

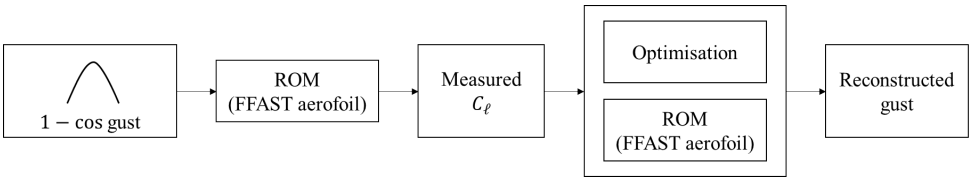

Figure 14: Gust reconstruction diagram

[15] Simeone, S., Agostinelli, C., Rendall, T., et al. (2016). Gust reconstruction from digital flight data recorder via numerical optimisation. In *57th AIAA/ASCE/AHS/ASC Structures, Structural Dynamics, and Materials Conference*. Reston, Virginia: American Institute of Aeronautics and Astronautics. ISBN 978-1-62410-392-6, pp. 1–19. doi:10.2514/6.2016-1484.

[16] Masters, D., Poole, D., Taylor, N., et al. (2017). Influence of shape parameterisation on a benchmark aerodynamic optimisation problem. *Journal of Aircraft*. ISSN 0021-8869.

[17] Hicks, R. M. and Henne, P. A. (1978). Wing Design by Numerical Optimization. *Journal of Aircraft*, 15(7), 407–412. doi:10.2514/3.58379.

[18] Wu, H. H.-Y., Yang, S., Liu, F., et al. (2003). Comparison of three geometric representations of airfoils for aerodynamic optimization. *16th AIAA Computational Fluid Dynamics Conference, Orlando, Florida*, (June). doi:10.2514/6.2003-4095.

[19] Katz, J. and Plotkin, A. (2001). *Low-Speed Aerodynamics*. Cambridge Aerospace Series. Cambridge University Press. ISBN 9780521665520.

[20] Wales, C., Jones, D., and Gaitonde, A. (2013). Reduced order modelling for aeroelastic aerofoil response to a gust. In *51st AIAA Aerospace Sciences Meeting*. Denver, USA: American Institute of Aeronautics and Astronautics, pp. 1–16.

[21] Jones, D. and Gaitonde, A. (2011). Future Fast Methods for Loads Calculations: The FFAST Project. In *Innovation for Sustainable Aviation in a Global Environment Proceedings of Aerodays*. Madrid, Spain: IOS Press BV, pp. 110–115.

[22] Williams, S. P., Jones, D., Gaitonde, A., et al. (2017). Reduced order modelling of aircraft gust response for use in early design stages. In *35th AIAA Applied Aerodynamics Conference, American Institute of Aeronautics and Astronautics*. Denver, USA: American Institute of Aeronautics and Astronautics.

[23] Juang, J.-N. and Pappa, R. S. (1985). An eigensystem realization algorithm for modal parameter identification and model reduction. *Journal of Guidance Control and Dynamics*, 8, 620–627.

[24] Wales, C., Gaitonde, A., and Jones, D. (2013). Stabilisation of reduced order models via restarting. *International Journal for Numerical Methods in Fluids*, 73(6), 578–599. ISSN 1097-0363. doi:10.1002/fld.3814.

[25] McKelvey, T., Akcay, H., and Ljung, L. (1996). Subspace-based multivariable system identification from frequency response data. *IEEE Transactions on Automatic Control*, 41(7), 960–979. ISSN 0018-9286. doi:10.1109/9.508900.

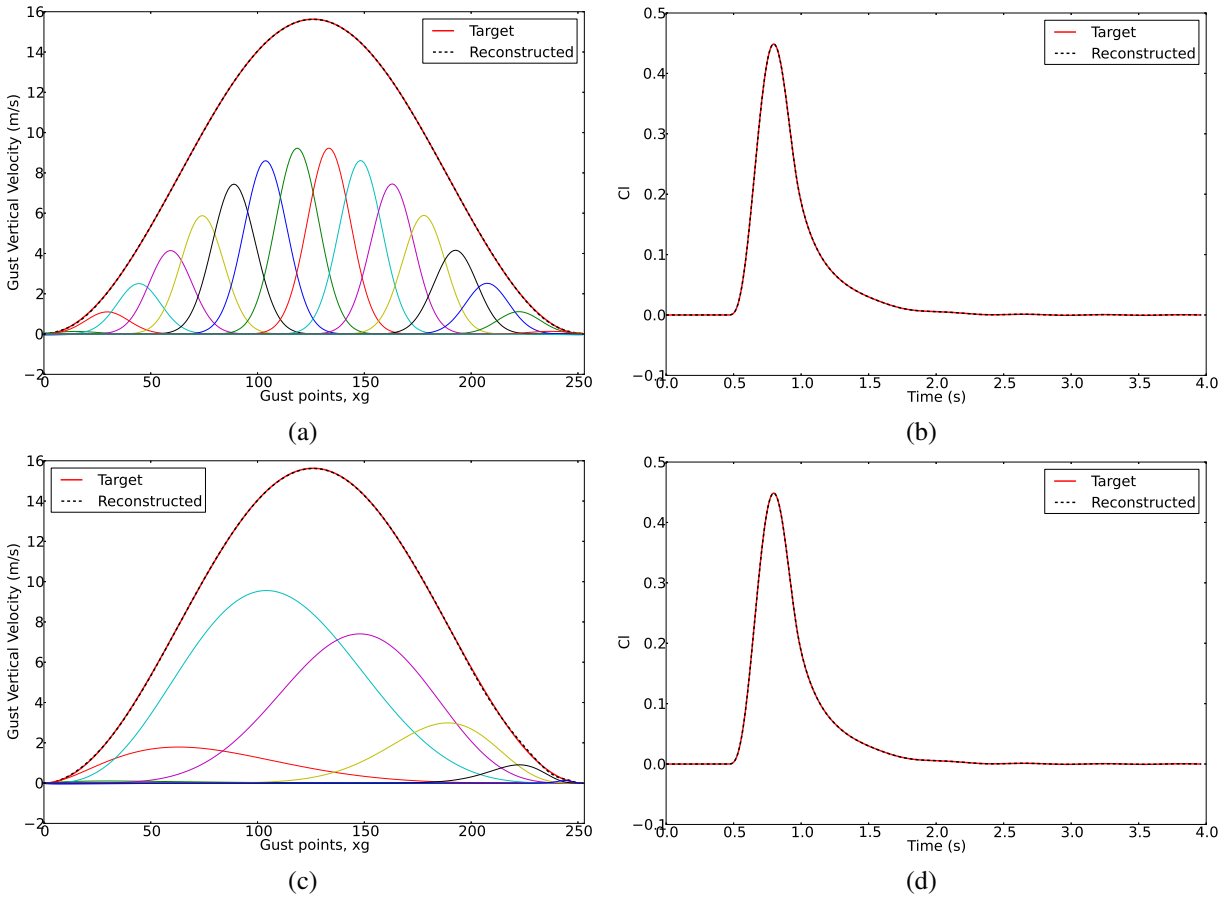

Figure 15: Reconstruction of gust profiles for the FFAST aerofoil ROM obtained with the SLSQP optimisation algorithm. Figures (a) and (b) show, respectively, the reconstructed gust and the resulting lift coefficient using 18 RBFs for the parameterisation. Figures (c) and (d)instead show, respectively, the reconstructed gust and the resulting lift coefficient using only 8 HHBFs for the parameterisation.

[26] Kraft, D. (1988). *A Software Package for Sequential Quadratic Programming*. Deutsche Forschungs- und Versuchsanstalt für Luft- und Raumfahrt Köln: Forschungsbericht. Wiss. Berichtswesen d. DFVLR.

[27] Simeone, S., Rendall, T., and Da Ronch, A. A gust reconstruction framework applied to a nonlinear reduced order model of a wing typical section. In *58th AIAA/ASCE/AHS/ASC Structures, Structural Dynamics, and Materials Conference*. Grapevine, Texas, USA: American Institute of Aeronautics and Astronautics. ISBN 978-1-62410-392-6, pp. 1–16. doi:10.2514/6.2017-0634.

COPYRIGHT STATEMENT